PAPER

Check for updates

Large-area all-perovskite-based coplanar photoelectrodes for scaled-up solar hydrogen production†

Wooyong Jeong,‡ Gyumin Jang,‡ Juwon Yun, Chang-Seop Jeong, Young Sun Park, Hyungsoo Lee, Jaehyun Son, Chan Uk Lee, Jeongyoub Lee, Junwoo Lee, Seongyeon Yang, Soobin Lee, Subin Moon and Jooho Moon [ID] *

Recently, lead halide perovskites (LHPs) have been intensively investigated for use as photoelectrodes in photoelectrochemical (PEC) water splitting systems, and PEC water splitting systems with LHP electrodes have shown outstanding solar-to-hydrogen (STH) efficiencies. Despite the significant role of large-scale deployment for practical commercialization, the fabrication of large-area LHP photoelectrodes is rarely investigated in the field of PEC water splitting. Herein, we present a strategy involving immersing an as-coated LHP film in an antisolvent containing cyclohexylammonium iodide (CHAI) for the fabrication of high-quality large-size LHP films for use in unbiased PEC water splitting. CHAI molecules accelerate nucleation kinetics by participating in the formation of an intermediate phase, resulting in uniform high-crystallinity LHP films. Furthermore, CHAI molecules effectively passivate grain boundaries, thereby increasing the photocurrent density and onset potential of PEC devices. Consequently, parallely illuminated coplanar LHP-based photoelectrodes with dimensions of 8 cm × 8 cm could be stably operated without any applied bias, and they exhibited a record-high STH efficiency of 9.89% and a T_{80} (the time at which the photocurrent density drops to 80% of its initial value) of 24 h. The hydrogen production rate of our device was 145.56 μmol h^{-1} cm^{-2}, which is highly comparable with previously reported values of state-of-the-art unassisted PEC devices.

Broader context

Recently, LHP-based integrated photoelectrodes have enabled efficient unbiased PEC water splitting. However, large-area photoelectrodes based on LHP films are rarely investigated. The introduction of the CHAI bathing method enables the fabrication of uniform large-scale LHP films with high crystallinity, whose grain boundaries are effectively passivated. Parallely illuminated coplanar LHP-based electrodes with dimensions of 8 cm × 8 cm exhibit a high STH efficiency of 9.89% under unbiased conditions with notable stability. The coplanar device achieves a hydrogen production rate of 145.56 μmol h^{-1} cm^{-2}, which is greater than all the previously reported values for PEC devices.

Introduction

Photoelectrochemical (PEC) water splitting is a promising technology for directly converting solar energy into easily storable green hydrogen (H$_2$).[1-3] Over the past few decades, various strategies such as morphology control, band alignment, and interfacial engineering have been used for fabricating

Department of Materials Science and Engineering, Yonsei University, Seoul 03722, Republic of Korea. E-mail: jmoon@yonsei.ac.kr

† Electronic supplementary information (ESI) available. See DOI: https://doi.org/10.1039/d4ee01167h

‡ These authors contributed equally.

photoelectrodes for PEC water splitting systems.[2,4-11] Yet, the use of PEC devices is not widespread because of their high fabrication cost, low performance and poor stability, along with the absence of large-scale deployment.[12] Recently, the development of lead halide perovskite (LHP)-based integrated photoelectrodes has helped overcome these drawbacks and has facilitated unbiased PEC water splitting, resulting in the achievement of a high solar-to-hydrogen (STH) efficiency exceeding 13% with high stability, encouraged by various encapsulation methods.[13-20] In particular, the solution processability of LHPs renders them suitable for large-scale and low-cost fabrication, as extensively pursued in the field of photovoltaics.[21-23] However, the fabrication of large-area LHP photoelectrodes has not been well investigated

This journal is © The Royal Society of Chemistry 2024

in the field of PEC water splitting. In particular, the light absorber's size is mostly below 1 cm^2, which is insufficient for the commercialization of LHP-photoelectrode-based PEC water splitting systems.[24,25] As the photoelectrodes account for a significant portion of the levelized cost of hydrogen, it is imperative to develop an LHP-based scalable PEC water splitting device.

The antisolvent dripping method often leads to severe irregularities when applied to large-area substrates, although it is widely utilized for preparing LHP films on a laboratory scale.[22] Recently, antisolvent bathing has emerged as an effective method for scaled-up fabrication of uniform LHP films.[26–29] This method has wide applicability and is simple, which is evident from its widespread use in the roll-to-roll coating process.[22,29,30] However, although as-coated wet films are fully submerged in an antisolvent bath, the time to reach supersaturation may be different for each location in the films. Such inhomogeneous nucleation may lead to irregularities in grain size and crystal orientation, which would generate defects along grain boundaries and thereby impede charge transport during the operation. Therefore, in the fabrication of large-scale LHP films through antisolvent bathing, apart from ensuring a constant nucleation rate, the passivation of defects should be carefully considered.

Despite the importance of defect passivation, reliable fabrication methods involving defect passivation are limited for large-scale LHP films. The most widely used methodology for interface and grain boundary passivation involves dripping an isopropyl alcohol (IPA) solution containing organic molecules during the spin coating of the perovskite precursor.[31,32] However, it is difficult to use this dripping method for large-area LHP films owing to the incomplete and nonuniform coverage of the film. Here, we propose a novel defect passivation strategy in which the as-coated LHP film is immersed in an antisolvent containing a passivation additive; the strategy is suitable for large-size-LHP-based unbiased PEC water splitting. In this strategy, an as-coated LHP film with a size of 8 cm × 8 cm is submerged in a bath of diethyl ether (DEE) antisolvent containing cyclohexylammonium iodide (CHAI) to not only induce rapid nucleation but also passivate the grain boundaries. This enhances the quality of the large-area film. A systematic chemical analysis confirmed that CHAI participates in the formation of an intermediate phase and enhances the crystallinity of the LHP film while simultaneously passivating the defects, thereby increasing the photocurrent density and onset potential of PEC devices. Parallelly illuminated coplanar LHP-based photoelectrodes were successfully operated without any applied bias, and they showed a maximum STH efficiency of 9.89% while maintaining 79% of their initial performance after 24 h. The H$_2$ production rate of the coplanar device was 145.56 μmol h^{-1} cm^{-2}, which is comparable with previously reported values of state-of-the-art unbiased PEC water splitting devices.

Results and discussion

Large-scale LHP films were fabricated using the antisolvent bathing method, as schematically illustrated in Fig. S1 (ESI†). A yellowish solution was prepared by dissolving a stoichiometric amount of perovskite precursor in a mixed solvent of N,N-dimethylformamide (DMF) and 1-methyl-2-pyrrolidinone (NMP). Subsequently, the precursor solution was spin-coated onto glass/fluorine-doped tin oxide (FTO)/SnO$_2$ substrates. For the preparation of the control sample, the as-coated wet films were immediately submerged in an antisolvent bath of DEE without any additive. During the bathing process, the antisolvent extracts the precursor solvents retained in the wet precursor film via inward diffusion owing to its miscibility. As the precursor solvents are replaced with the antisolvent, the color of the wet film gradually changes from yellow to transparent brown as the crystallization initiates. For antisolvent bathing involving an additive, IPA containing dissolved CHAI was added to the DEE bath (the associated bathing process is hereafter referred to as CHAI bathing). CHAI molecules were selected to boost the passivation capability of the LHP film induced by the localized electron density in cyclohexylamine.[33] In the case of CHAI bathing, the color change was significantly accelerated, which was indicative of rapid nucleation. After the bathing process, the retrieved films were annealed at 100 °C on a hotplate for 60 min under ambient conditions.

Digital photographs of LHP films before and after annealing were obtained to visually compare the surface finish. As shown in Fig. S2 (ESI†), the control film before annealing exhibited a highly rough surface because of uncontrolled crystallization kinetics. Such an irregular morphology was observed even after annealing. By contrast, annealed CHAI-bathed films showed a significantly enhanced morphology, with a smooth surface. A scanning electron microscopy (SEM) image of the control film clearly showed an uneven and rough microstructure (Fig. 1(a)). For conventional antisolvent bathing, sluggish solvent extraction likely leads to uncontrolled nucleation and growth, resulting in significant thickness variations (Fig. 1(c)). By contrast, the CHAI-bathed LHP films showed a smooth surface morphology (Fig. 1(b)). Their flat surface and uniform thickness were also confirmed from a cross-sectional SEM image (Fig. 1(d)). Such a smooth surface finish results from accelerated crystallization kinetics, which leads to homogeneous crystallization over the entire film. Atomic force microscopy (AFM) topography was utilized to calculate the root-mean-square roughness (Fig. S3, ESI†). The control film's surface roughness was 28.9 nm, and it decreased drastically to 16.6 nm when CHAI bathing was employed.

X-ray diffraction (XRD) spectra of the as-retrieved wet films obtained through conventional antisolvent bathing and CHAI bathing exhibited clear diffraction peaks at 14.36° and 28.36°, corresponding to the (110) and (220) planes of (FAPbI$_3$)$_{0.95}$ (MAPbBr$_3$)$_{0.05}$, respectively (Fig. 1(e)). Notably, the wet precursor film obtained through CHAI bathing showed intense peaks for the (110) and (220) planes. The LHP film prepared through conventional antisolvent bathing showed a peak intensity ratio ($I_{(110)}/I_{(FTO)}$) of 7.95, whereas the CHAI-antisolvent-bathed film exhibited a significantly higher intensity ratio of 56.36, which confirmed accelerated crystallization kinetics. As evident in Fig. 1(f), both the annealed films showed a strong (110) plane that was slightly shifted to 14.14°. The control sample exhibited

This journal is © The Royal Society of Chemistry 2024

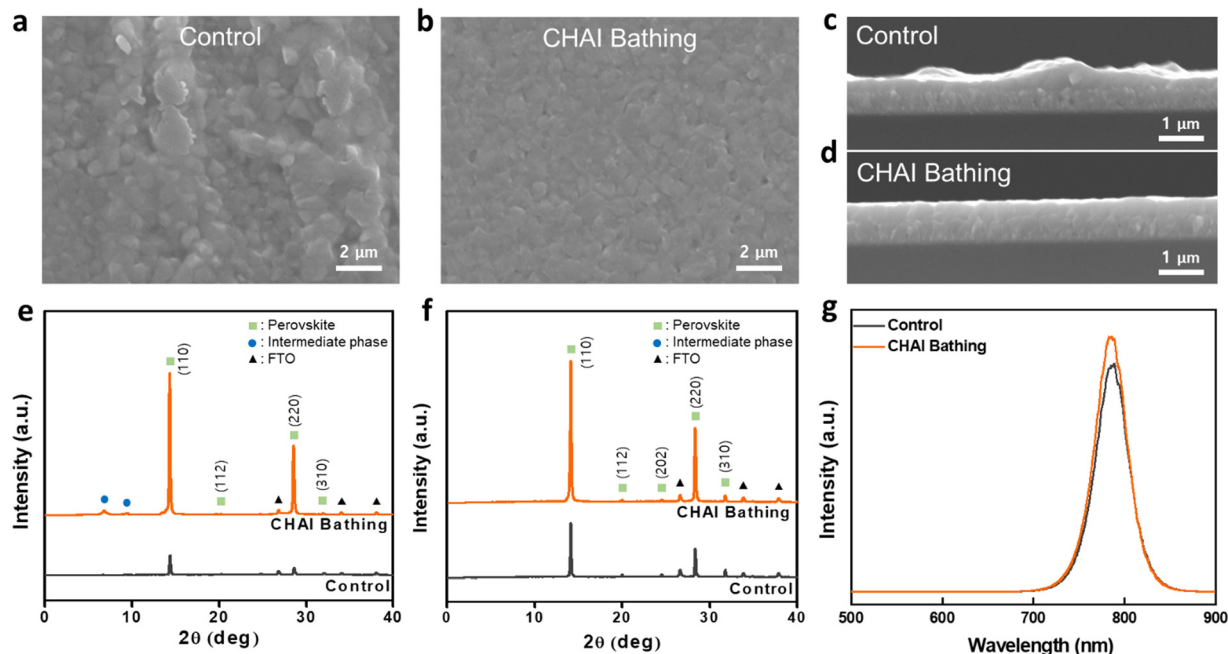*Energy Environ. Sci.*, 2024, **17**, 3604–3617 | **3605**

Fig. 1 Top-view and cross-sectional SEM images of (a) and (c) control LHP films and (b) and (d) CHAI-bathed LHP films. XRD patterns of the control and CHAI-bathed LHP films (e) before and (f) after annealing and (g) steady-state PL spectra of the control and CHAI-bathed LHP films fabricated on glass/FTO/SnO$_2$.

a peak intensity ratio of 11.62, while the value of $I_{(110)}/I_{(FTO)}$ for the CHAI-antisolvent-bathed film was 29.97. XRD results indicated that CHAI molecules were involved in rapid crystallization, which enhanced the crystallinity of perovskite films. Furthermore, the peak intensity ratio $I_{(110)}/I_{(310)}$ was compared for the control and CHAI-antisolvent-bathed films to identify any differences in the preferred crystal orientation.[34] These two films showed peak intensity ratios of 6.98 and 18.48, respectively, indicating a significant preferred orientation of the (110) perovskite plane for the CHAI-bathed film.

To further understand the effect of CHAI bathing on the optical properties of the CHAI-antisolvent-bathed LHP film, steady-state photoluminescence (PL) was measured (Fig. 1(g)). Both samples exhibited a strong PL peak at a wavelength of about 783 nm, which corresponds to the bandgap of (FAPbI$_3$)$_{0.95}$(MAPbBr$_3$)$_{0.05}$. Interestingly, the CHAI-antisolvent-bathed sample showed a slightly more intense PL peak compared to the control sample. It is noteworthy that neither the bandgap difference nor the PL peak of a 2D perovskite phase was observed for the CHAI-bathed samples. It has been reported that CHAI molecules can interact with the wet precursor film to form a 2D Ruddlesden–Popper perovskite phase.[33] However, the absence of a 2D phase in PL analysis suggests that CHAI molecules resided at the grain boundary or surface of films without being embedded in the perovskite lattice. A PL mapping image was obtained to further confirm the optical homogeneity (Fig. S4, ESI†). The control sample showed a broad PL peak distribution between 780 and 792 nm, suggesting optical inhomogeneity due to locally uneven stoichiometry, which might be induced by tremendous defect density. On the other hand, the CHAI-bathed sample showed

an extremely narrow PL peak distribution, ranging from 778 to 783 nm, indicative of a reduced defect density and locally even stoichiometry.

The interaction between CHAI and the precursor during the bathing process played an important role in determining the crystallization kinetics of the LHP film. Before annealing, both control and CHAI-antisolvent-bathed wet precursor films showed additional diffraction peaks at low 2θ angles (Fig. 2(a) and (b)). The control film exhibited distinct peaks at $6.66°$, $7.12°$, $8.90°$, and $9.24°$, all of which indicated the presence of formamidinium iodide (FAI)–PbI$_2$–DMF or FAI–PbI$_2$–NMP intermediate phases.[35–38] The CHAI antisolvent-bathed sample also contained an FAI-PbI$_2$-NMP intermediate phase, which was indicated by diffraction peaks at $8.92°$ and $9.26°$. However, the additional peak at $6.84°$ cannot be assigned to intermediate phases (i.e., FAI–PbI$_2$–DMF and FAI–PbI$_2$–NMP) or to a 2D perovskite phase (n = 1, CHA$_2$PbI$_4$).[33] This peak suggests that an unidentified intermediate phase was produced during the film's immersion in the antisolvent bath containing CHAI. In order to determine the origin of the diffraction peak at $6.84°$, CHAI–PbI$_2$–NMP, CHAI–PbI$_2$–DMF, CHAI–FAI–PbI$_2$–NMP, and CHAI–FAI–PbI$_2$–DMF samples were prepared, and their XRD spectra were obtained (Fig. S5, ESI;† see the Experimental Section for details of sample preparation). Interestingly, the CHAI–PbI$_2$–NMP and CHAI–FAI–PbI$_2$–NMP intermediates exhibited a diffraction peak at $6.84°$, similar to the CHAI-bathed sample. Therefore, CHAI molecules were involved in the formation of the additional intermediate phase, and they competitively occupied the positions of FA$^+$ cations, which could have accelerated the crystallization kinetics. Fourier-transform infrared (FTIR) spectra of CHAI-bathed films prior

3606 | *Energy Environ. Sci.*, 2024, **17**, 3604–3617

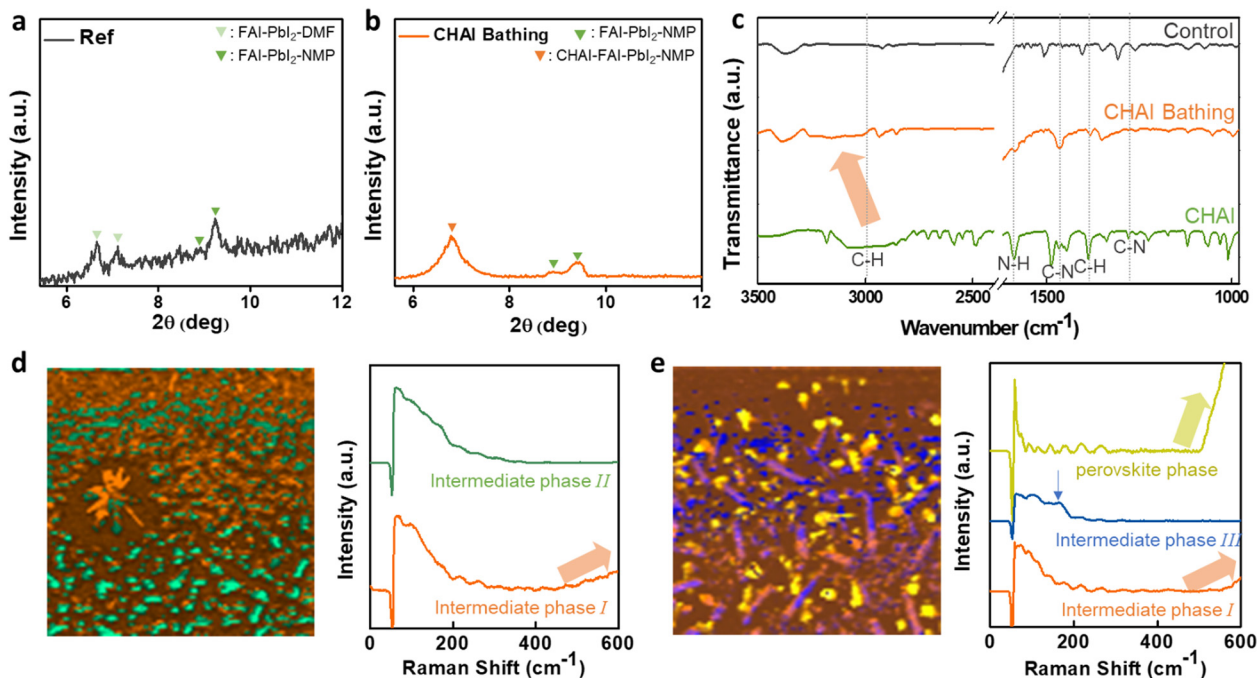This journal is © The Royal Society of Chemistry 2024

Fig. 2 XRD patterns of the (a) as-bathed control and (b) CHAI-bathed LHP films. (c) FTIR spectra of as-retrieved control and CHAI-bathed films before annealing as well as of pristine CHAI powder. Raman mapping images and spectra of (d) control and (e) CHAI-bathed films, used to determine the phase spatial distribution. The different phases were labeled intermediate phase I (orange), intermediate phase II (green), intermediate phase III (blue), and the perovskite phase (yellow).

to annealing showed vibrations similar to those of pristine CHAI powder (*i.e.*, the aromatic C–H stretching mode (2900–3100 cm^{-1}), N–H bending mode (1591 cm^{-1}), C–N stretching mode (1487 cm^{-1}), C–H symmetric deformation mode (1388 cm^{-1}), and C–N stretching mode (1281 cm^{-1})), which indicated the incorporation of CHA$^+$ ions into the new intermediate phase (Fig. 2(c)).[39] It is noteworthy that the aromatic C–H stretching mode at 2900–3100 cm^{-1} observed for the CHAI-bathed film was slightly shifted toward higher wavenumbers compared to that observed for pristine CHAI powder, indicating that CHAI participated in the intermediate phase's formation.

Raman mapping images were obtained to investigate the spatial distribution of the intermediate phases before annealing (Fig. 2(d) and (e)). The scanned area of the control sample was mostly covered with intermediate phase I (orange), which is speculated to be a mixture of FAI–PbI$_2$–NMP and FAI–PbI$_2$–DMF phases. It should be noted that the signal intensity of intermediate phase I (orange) slightly increased at high wavenumbers.[40,41] Such an increase in intensity may indicate that the intermediate phases slowly transitioned toward the black perovskite phase, consistent with the steady-state PL spectra (Fig. S6, ESI†).[42] At low wavenumbers, intermediate phase II (green) showed Raman peaks identical to those of intermediate phase I, and at high wavenumbers, there was no increase in the Raman signal. On the other hand, the Raman mapping image of the CHAI-antisolvent-bathed sample exhibited three different phases, including intermediate phase I (orange). A black perovskite phase (yellow) with significantly high intensity was also observed at high wavenumbers (>550 cm^{-1}) owing to its strong PL signal.[40,41] The strong PL

signal was consistent with the steady-state PL measurement of CHAI-bathed films before annealing (Fig. S6, ESI†). The observation of the black perovskite phase indicates that crystallization kinetics were accelerated when CHAI bathing was employed. Furthermore, a uniformly distributed phase (blue) emerged (hereafter referred to as intermediate phase III). It is speculated that this new phase likely resulted from the CHAI-involved intermediate phase. To support our hypothesis, we obtained the Raman spectrum of a wet film prepared from the CHAI–FAI–PbI$_2$–NMP intermediate phase; the Raman spectrum is shown in Fig. S7 (ESI†). The Raman spectrum was identical to that of intermediate phase III, confirming that intermediate phase III resulted from CHAI incorporation during the antisolvent bathing. It can be inferred that CHAI bathing led to the formation of a new intermediate phase because CHAI molecules competitively occupied the positions of FA$^+$ cations, which accelerated the crystallization kinetics.

According to the LaMer model, the nuclei start to evolve when the concentration of the precursor solution reaches the supersaturation concentration (C_S) (Fig. S8, ESI†). The precursor concentration gradually decreases with nucleus formation, and eventually nucleation is terminated when the concentration drops below C_S. In particular, all the nuclei start growing spontaneously immediately after their formation, and they grow until all reactants are consumed. In the case of the control film, the precursor concentration remained above C_S for a long time because of the slow crystallization kinetics. Therefore, additional nuclei were continuously formed while the evolved perovskite nuclei grew during bathing, resulting in

This journal is © The Royal Society of Chemistry 2024

Energy Environ. Sci., 2024, **17**, 3604–3617 | **3607**

an uncontrolled perovskite crystal size with poor uniformity of the final film. By contrast, the perovskite precursor underwent rapid nucleation when CHAI bathing was employed, which abruptly decreased the precursor concentration below C_S. Hence, nucleation was terminated almost immediately after bathing, and most nuclei grew concurrently. Consequently, highly uniform perovskite films with a larger grain size and lower roughness could be obtained.

The presence of CHAI molecules in the annealed perovskite film was verified using proton nuclear magnetic resonance (^{1}H-NMR) spectroscopy; a CHAI-bathed LHP film dissolved in DMSO-d_6 solvent was used for the purpose. As shown in Fig. S9 (ESI†), chemical shifts were detected at 1.26, 1.58, 1.62, 1.73, and 1.90 ppm, confirming the presence of CHA$^+$ ions. Furthermore, the elemental depth profile was obtained using time-of-flight secondary ion mass spectroscopy (ToF-SIMS) to examine the distribution of cations (*i.e.*, $CH_3NH_3^+$ (MA$^+$), CHA$^+$, Cs$^+$, Sn$^+$, and Pb^{2+}) and anions (*i.e.*, I$^-$ and Br$^-$) on the annealed CHAI-antisolvent-bathed LHP film. As shown in Fig. 3(a), CHA$^+$ ions were confirmed to be present and uniformly distributed
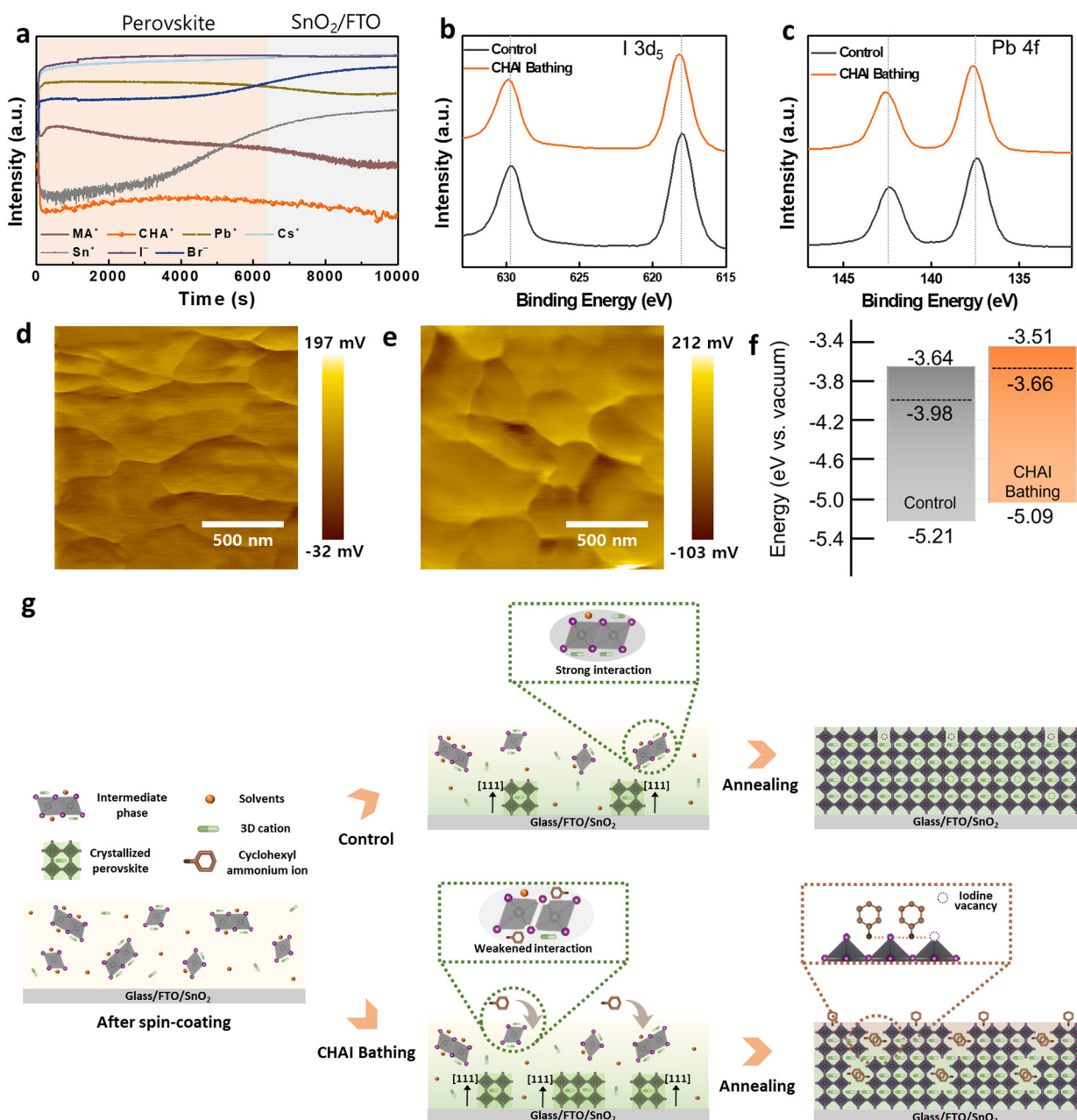

Fig. 3 (a) ToF-SIMS depth profiles of CHAI-bathed LHP films deposited on glass/FTO/SnO$_2$ substrates. (b) I 3d$_5$ and (c) Pb 4f XPS spectra of the control and CHAI-bathed LHP films, respectively. The contact potential difference between the grain interiors and grain boundaries for the (d) control and (e) CHAI-bathed LHP films is also shown. (f) Band energy level of the control and CHAI-bathed LHP films. (g) Schematic of the crystallization mechanism in the CHAI bathing method.

3608 | *Energy Environ. Sci.*, 2024, **17**, 3604–3617

This journal is © The Royal Society of Chemistry 2024

throughout the perovskite film. Furthermore, the interaction between CHAI and Pb–I frameworks was investigated using FTIR spectroscopy (Fig. S10, ESI†). The annealed CHAI-antisolvent-bathed film showed aromatic C–H stretching peaks (2900–3100 cm^{-1}), N–H bending peaks (1591 cm^{-1}), C–N stretching peaks (1487 cm^{-1}), C–H symmetric deformation peaks (1388 cm^{-1}), and C–N stretching peaks (1281 cm^{-1}) owing to the incorporation of CHA$^+$ ions. The positions of these peaks were slightly shifted relative to those of the characteristic peaks of pristine CHAI powder, indicating interaction between CHA$^+$ ions and Pb–I frameworks.[35,43,44]

To verify the location of CHAI molecules in the annealed film, we performed Kelvin probe force microscopy (KPFM) with control and CHAI-bathed LHP films deposited onto glass/FTO. KPFM is useful for acquiring nanoscale spatial information on the basis of contact potential difference. The change in the work function of the surface of the sample being inspected can be determined from the variation in the contact potential difference. A higher contact potential difference indicates a higher work function in a given region. Fig. 3(d) and (e) show contact potential difference maps for the control and CHAI-treated perovskite thin films, respectively. Under dark conditions, the measured contact potential difference at the grain boundaries was generally higher than that in the grain interior, as indicated by the bright edge boundaries.[34] It can be observed that the averaged difference between the grain boundary and grain interior significantly increased from 95 mV (for the control sample) to 140 mV for the CHAI-bathed LHP film. Such an increase in the work function clearly indicates the presence of CHAI at the grain boundaries.

X-ray photoelectron spectroscopy (XPS) was used to identify the location of CHAI molecules in perovskite frameworks. The I 3d$_5$ peak was found to have shifted toward a higher binding energy for the CHAI-antisolvent-bathed sample (Fig. 3(b)), suggesting that CHA$^+$ ions interacted with iodide ions in the Pb–I framework and suppressed iodine migration, thereby reducing trap states. It could be speculated that the CHA$^+$ ions functioned not only as surface dipoles, but also as grain boundary passivators. The Pb 4f peaks also shifted toward a higher binding energy, suggesting interaction between unsaturated Pb^{2+} and lone-pair electrons of CHA$^+$ (Fig. 3(c)).[45–49] It is speculated that CHA$^+$ acts as a Lewis base, donating electrons to Lewis acid (i.e., undercoordinated Pb^{2+}). By contrast, previous studies on the 2D/3D perovskite heterostructure have reported a shift in the Pb 4f peak toward lower binding energies when a 2D perovskite is formed.[33,50,51] Furthermore, XPS depth analysis was conducted from the surface to the bottom of the LHP films. Elemental depth profiles for the CHAI-bathed sample clearly showed an increase in the atomic percentage of C and N with respect to the control sample as a result of CHAI incorporation (Fig. S11, ESI†). XPS depth spectra obtained for different etching durations (i.e., 200–1200 s) are shown in Fig. S12 (ESI†) (entire XPS depth spectra are presented in Fig. S13, ESI†). With an increase in the etching duration, I 3d$_5$ and Pb 4f peaks shifted to higher binding energies for the CHAI-bathed samples. This implies that CHA$^+$ interacted with

Pb-I frameworks throughout the film, which is highly consistent with the ToF-SIMS result. It could also be confirmed that the CHA$^+$ ions were mainly located at grain boundaries of the LHP films and interacted with Pb-I frameworks without the formation of CHA$^+$-containing 2D perovskite.

We performed ultraviolet photoelectron spectroscopy (UPS) to determine the band energy level change resulting from the presence of CHA$^+$ ions (Fig. S14, ESI†). The Fermi level and valence band minimum of the control film were calculated to be −3.98 and −5.21 eV, respectively, and those of the CHAI-bathed sample were −3.66 eV and −5.09 eV, respectively, both of which were upshifted relative to the values for the control sample (Fig. 3(f)). This observation is highly consistent with a previous study in which grain boundary passivation by organic molecules caused an upshift in the band energy.[52] On the basis of our observation, we schematically illustrate the crystallization mechanism for the CHAI-bathed sample in Fig. 3(g). It can be conjectured that CHAI competitively participates in the formation of intermediate phases with FAI, weakening their bond strength. Hence, the crystallization kinetics could be accelerated when CHAI molecules are employed in the anti-solvent bath. After spin-coating the precursor solution, wet precursor films were submerged in the CHAI-added antisolvent bath. During the bathing process, it is believed that intermediate phase III was rapidly formed through the participation of CHA$^+$ ions into the intermediate phases (i.e., I and II), competing for PbI$_6^{4-}$ interaction with other cations (i.e., FA$^+$, MA$^+$, and Cs$^+$). Since the perovskite crystal nucleated from intermediate phase III, CHA$^+$ ions could be incorporated at grain boundaries, effectively passivating uncoordinated Pb^{2+} ions and resulting in the preferred orientation of the perovskite crystal.

The effect of the enhanced morphology and preferred orientation after CHAI bathing on a perovskite solar cell's (PSC's) performance was determined. The n–i–p structured PSC had a device configuration of glass/FTO/SnO$_2$ ($\sim$20 nm)/LHP ($\sim$500 nm)/2,2′,7,7′-tetrakis(N,N-di-4-methoxyphenylamino)-9,9′-spirobifluorene (spiro-OMeTAD, $\sim$150 nm)/Au (80 nm), and it is schematically shown in Fig. S15 (ESI†). First, the current density of the PSCs was measured through a negative voltage scan under 3 A grade simulated air mass (AM) 1.5 G 100 mW cm^{-2} irradiation (Fig. 4(a)). The photovoltaic parameters of the control and CHAI-treated PSCs are listed in the inset of Fig. 4(a). The control device based on a conventionally bathed LHP film exhibited a champion power conversion efficiency (PCE) of 17.42%, with an open-circuit voltage (V_{OC}) of 1.03 V, a short-circuit current density (J_{SC}) of 23.29 mA cm^{-2}, and a fill factor (FF) of 72.90%. By contrast, the PSC based on CHAI-bathed LHP films showed an improved PCE of 21.35%, with J_{SC} = 23.27 mA cm^{-2}, V_{OC} = 1.12 V, and FF = 82.10%. The photovoltaic parameter statistics obtained for 16 samples are presented in Fig. S16 (ESI†). For conducting the ambient stability test, we stored the fabricated devices under atmospheric conditions without encapsulation at a relative humidity of 30 ± 10%. The normalized PCE was plotted against the storage time (Fig. 4(b)). After being exposed to ambient conditions for 1350 h, the control device showed considerable
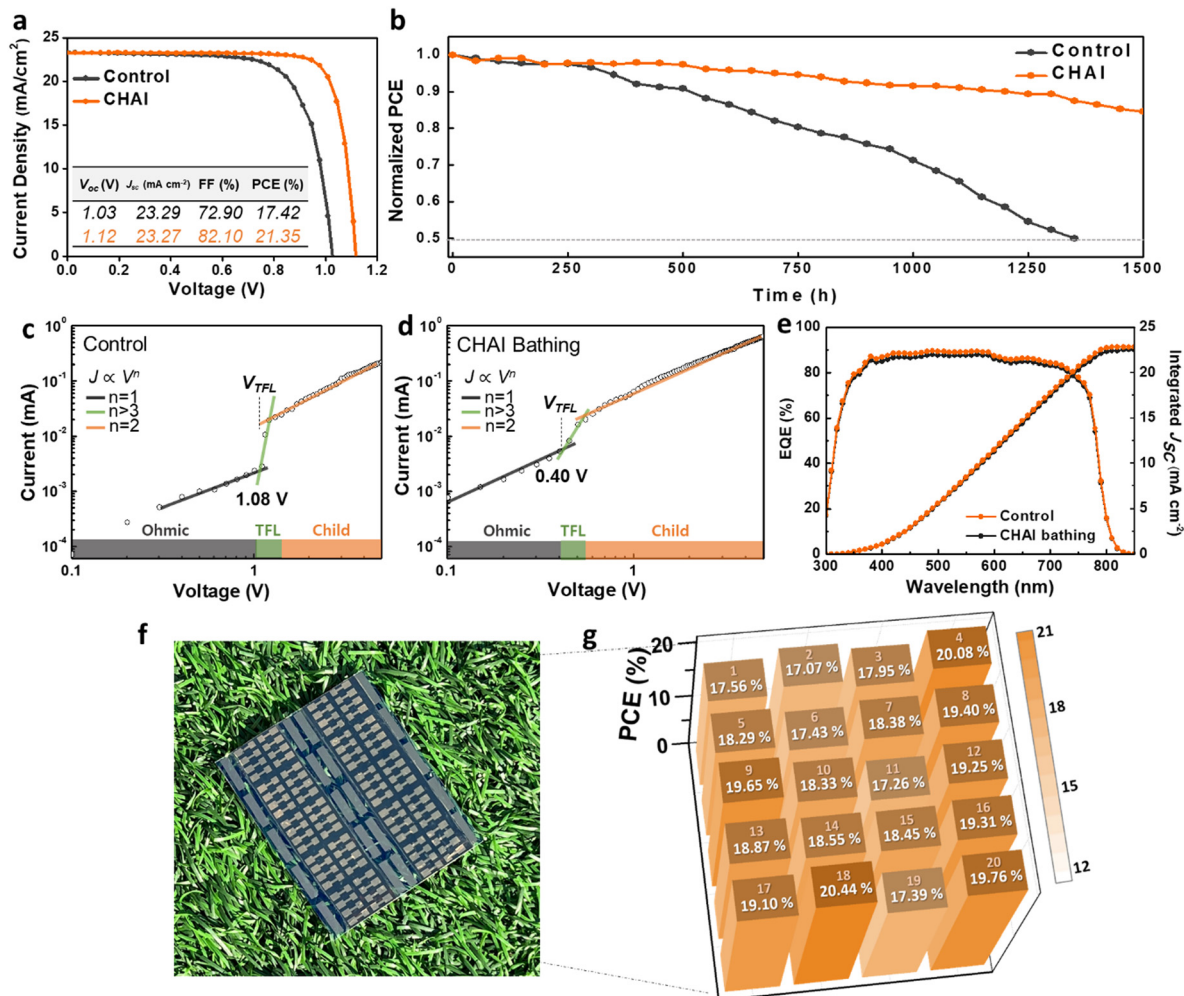
This journal is © The Royal Society of Chemistry 2024

Energy Environ. Sci., 2024, **17**, 3604–3617 | **3609**

Fig. 4 Photovoltaic properties of PSCs fabricated with each LHP film. (a) J–V curves of control and CHAI-bathing-derived PSCs under AM 1.5G illumination using a 0.06 cm^2 metal aperture mask. (b) Normalized PCE of PSCs prepared with control and CHAI-bathed LHP films under a relative humidity of $30 \pm 10\%$ (*i.e.*, ambient stability). Dark current–voltage curves of (c) control and (d) CHAI-bathed films, used for SCLC measurements. (e) EQE spectra and integrated J_{SC} of PSCs fabricated with different bathing methods. (f) A photograph of the large-area LHP films (8 cm × 10 cm) prepared with the CHAI-bathing method. (g) A three-dimensional plot of the PCE values of PSCs depending upon the position of 20 sub-cells.

degradation, retaining only 50.0% of its original PCE. On the other hand, the CHAI-bathed PSCs maintained over 84.5% of their initial PCE even after 1500 h. It appears that the superior photovoltaic performance and enhanced stability of the CHAI-bathed PSCs resulted from efficient charge transport without charge accumulation, associated with the improved film morphology and preferred orientation of perovskite crystals.

To gain an understanding of the V_{OC} enhancement, we determined the trap density for the device configuration glass/FTO/LHP film/Au through space charge-limited current (SCLC) analysis. It has been reported that the ion migration associated with the voltage sweep during the SCLC measurement could adversely affect defect density evaluation.[53,54] Therefore, a voltage pulse of 5 V was applied for 1 min prior to SCLC analysis. For both LHP films, no noticeable difference between the negative and positive scan directions was observed (Fig. S17, ESI†). Thus, it was confirmed that ion migration hardly affected the density of defects measured through the

SCLC approach. J–V curves, shown in Fig. 4(c) and (d), were measured under dark conditions, and they exhibited three regions depending on the slope of the curve, namely, Ohmic, trap-filled, and child regions. In the Ohmic regime across low voltages, the current increased linearly with the voltage owing to the Ohmic response. As the voltage further increased, the current showed a rapid exponential increase, indicating that all the available trap states were filled with injected carriers; this region is referred to as the trap-filled limit region. The voltage value between the Ohmic and trap-filled regions is termed trap-filled limit voltage (V_{TFL}), and it can be used for calculating the trap density in LHP films. The trap density (n_{trap}) can be calculated from the following equation:

$$V_{TFL} = \frac{e n_{trap} L^2}{2 \varepsilon \varepsilon_o} \tag{1}$$

where L is the thickness of perovskite films, ε is the permittivity of the perovskite, and ε_o is the vacuum permittivity. The V_{TFL}

3610 | *Energy Environ. Sci.,* 2024, **17**, 3604–3617

This journal is © The Royal Society of Chemistry 2024

values were determined to be 1.08 and 0.40 V for the control and CHAI-bathed LHP films, respectively, and the corresponding n_{trap} was calculated to be 2.46×10^{15} and 9.12×10^{14} cm^{-3}, respectively. The 63% reduction in the trap density for the CHAI-antisolvent-bathed films apparently resulted from the defect passivation by CHA$^+$ ions at grain boundaries, which led to the significant V_{OC} enhancement. The external quantum efficiencies (EQEs) of both devices were measured, and the integrated current densities were 22.5 mA cm^{-2} for the control device and 22.8 mA cm^{-2} for CHAI-bathed devices, showing a negligible difference (less than 3.5%) with respect to the J_{SC} values obtained from J–V curves (Fig. 4(e)).

To examine the large-area compatibility of CHAI-based antisolvent bathing, large-area PSCs with dimensions of 8 cm × 10 cm were fabricated (Fig. 4(f)). The large-area device was divided into 20 sub-cells, each measuring 2 cm × 2 cm, to determine uniformity in terms of the PCE. As shown in the 3D plot of PCE values in Fig. 4(g), an average PCE of 18.63 ± 0.99% was achieved, and it indicated high homogeneity of the device performance over the large area. The champion cell exhibited a PCE of 20.44%, which was highly comparable to the PCE of the small-area counterpart. The J–V curves of the 20 sub-cells are presented in Fig. S18 (ESI†). In order to further confirm the compatibility of the proposed CHAI bathing with the scalable film deposition method, 8 cm × 10 cm-sized large-area LHP films were prepared through bar-coating (Fig. S19, ESI†) as demonstrated in Fig. S20(a) (ESI†). To determine the device-

level homogeneity of large-area perovskite films, the bar-coated films were divided into 20 subcells (2 cm × 2 cm) for fabricating solar cells. With the optimal coating condition, an average PCE of 18.61 ± 1.37% could be achieved from the 20 subcells, indicating excellent device parameters over the entire area (Fig. S20(b and c), ESI†). The bar-coating based champion cell exhibited a PCE of 21.44%, which is highly comparable to that of its spin-coating-based counterpart.

Next, a perovskite-based photoanode was fabricated for use in the oxygen evolution reaction (OER), by spreading conductive carbon powder over and attaching an Ni foil on top of the Au electrode to prevent water penetration to the LHP. Owing to the low OER catalytic activity of the Ni foil, hydrothermally synthesized NiFe-layered double hydroxide (NiFeLDH) deposited on Ni foam (denoted by NiFe-LDH@Ni foam) was used as an OER cocatalyst, and it was attached to the Ni foil (i.e., glass/FTO/SnO$_2$/LHP/spiro-OMeTAD/Au/carbon powder/Ni foil/NiFe-LDH@Ni foam; see Experimental Section for additional details). The best OER performance of the CHAI-bathed-perovskite-based photoanode with an active area of 0.8 cm^2 was determined using linear sweep voltammetry (LSV) under 1-sun illumination in 1 M KOH (pH 14). As evident in the LSV graph in Fig. 5(a), the prepared photoanode exhibited superior performance with an onset potential of 0.45 V_{RHE}, and the saturation photocurrent density was 24.1 mA m^{-2} at 1.23 V_{RHE}. The operational stability of the perovskite photoanode was evaluated by conducting chronoamperometry measurements
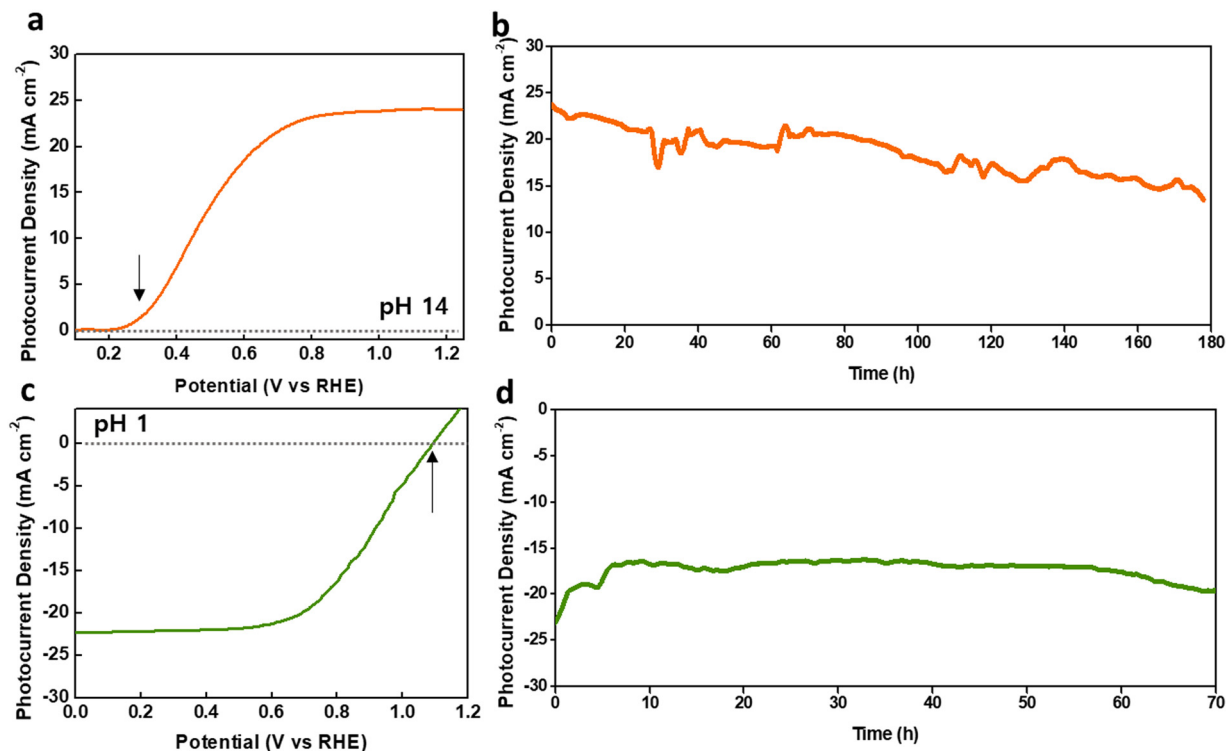

Fig. 5 (a) LSV curve of the photoanode with the configuration CHAI-bathed perovskite/Ni foil/NiFe-LDH@Ni foam in a 1 M KOH electrolyte (pH 14) and (b) the photocurrent density tracked at 1.23 V_{RHE} under 1-sun illumination. (c) LSV curve of the photocathode (i.e., CHAI-bathed perovskite/Pt catalyst with carbon black) in a 0.5 M H$_2$SO$_4$ electrolyte (pH 14) and (d) its photocurrent density stability at 0 V_{RHE}. All data were obtained under continuous 1-sun illumination.

at 1.23 V_{RHE} in a basic electrolyte with pH 14 under continuous illumination. As shown in Fig. 5(b), the photoanode showed noteworthy stability, retaining about 88% of its initial photo-current density after 24 h and about 62% after 175 h. In order to perform unbiased solar water splitting, a perovskite-based photocathode was also fabricated by positioning a Cu wire on the top electrode. In the case of the photocathode, the hydrogen evolution reaction (HER) at the catalyst/electrolyte interface, located at the physically remote bottom electrode, where Pt particles together with 20% carbon black were deposited onto FTO. The LSV measurement confirmed that the perovskite photocathode exhibited remarkable HER performance in
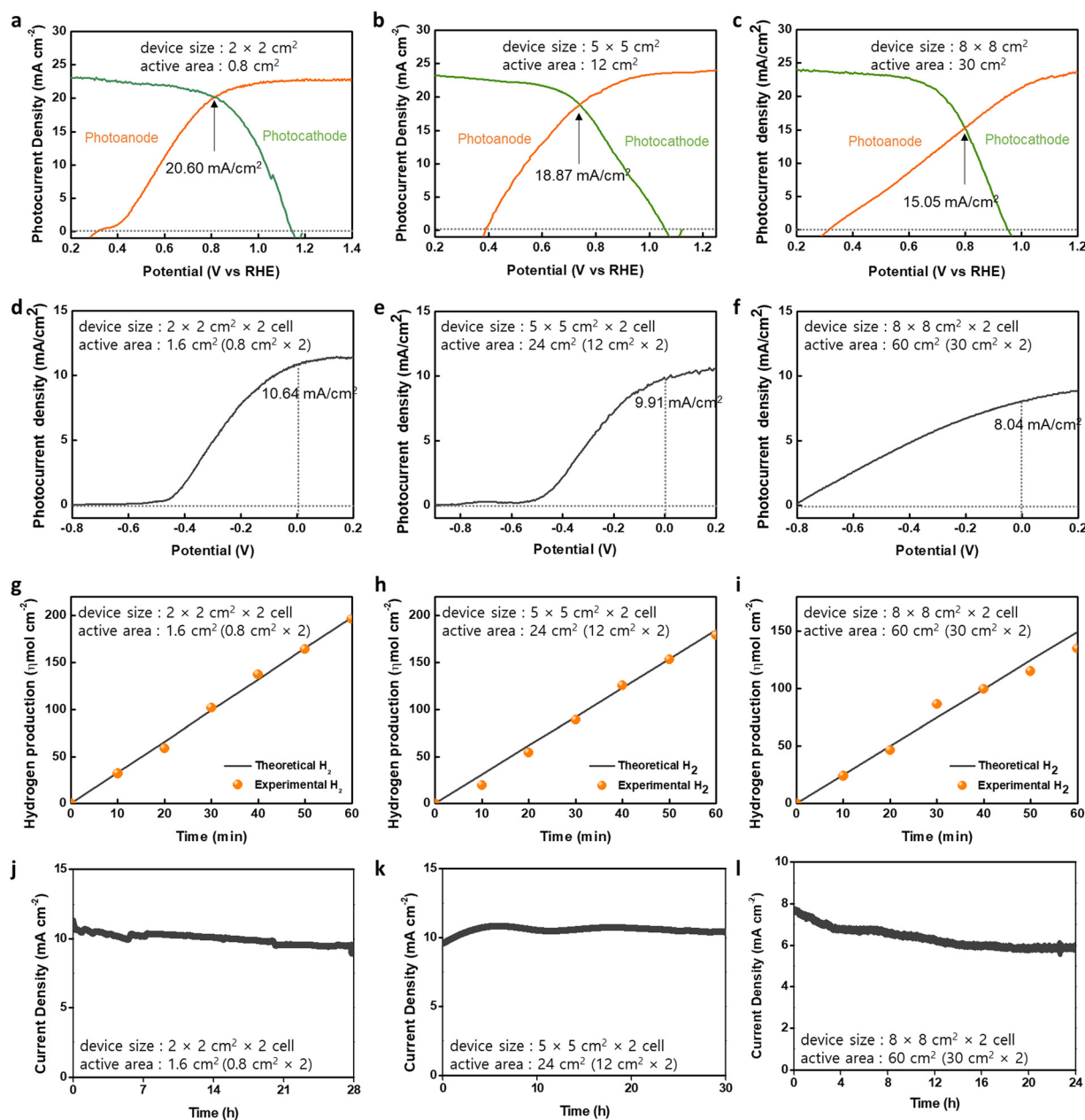

Fig. 6 (a)–(c) LSV curves for the perovskite/Ni foil/NiFe-LDH@Ni foam photoanode and perovskite/Pt carbon photocathode with device dimensions of 2 cm × 2 cm, 5 cm × 5 cm, and 8 cm × 8 cm, respectively (active area of 0.8 cm^2, 12 cm^2, and 30 cm^2, respectively). LSV curves are obtained under 1-sun illumination in 0.5 M KPi (pH 7). The operational point of the parallelly illuminated coplanar LHP-based photoelectrode was determined. (d)–(f) LSV curves of the parallelly illuminated coplanar LHP-based photoelectrodes (a photoanode and a photocathode) with an active area size of 1.6 cm^2, 24 cm^2, and 60 cm^2, respectively. LSV curves are obtained under 1-sun illumination in 0.5 M KPi (pH 7) under a two-electrode unbiased condition (0 V). (g)–(i) H$_2$ gas production rates as a function of operation time of the coplanar LHP-based photoelectrode with active area sizes of 1.6 cm^2, 24 cm^2, and 60 cm^2 under unbiased conditions. The solid line indicates the calculated H$_2$ production rate, and the circles represent the experimental (gas chromatography) values obtained at 10 min intervals. (j)–(l) Operational stability of parallelly illuminated coplanar LHP-based photoelectrodes with active area sizes of 1.6 cm^2, 24 cm^2, and 60 cm^2 obtained under 1-sun illumination in 0.5 M KPi (pH 7) without applied bias.

3612 | *Energy Environ. Sci.*, 2024, **17**, 3604–3617

This journal is © The Royal Society of Chemistry 2024

0.5 M H$_2$SO$_4$ (pH 1), with an onset potential of 1.12 V_{RHE} and a saturation photocurrent density of 23.0 mA m^{-2} at 0 V_{RHE} (Fig. 5(c)). The operational stability of the photocathode was further assessed by tracking the photocurrent density as a function of the elapsed time at 0 V_{RHE} in an acidic electrolyte of pH 1. As shown in Fig. 5(d), the photocathode exhibited no noticeable degradation after 24 h and maintained 80% of its photocurrent density after 70 h. Furthermore, the applied bias photon-to-current conversion efficiency (ABPE) was calculated to be 9.59% (at 0.79 V_{RHE}) and 13.93% (at 0.71 V_{RHE}) for the photoanode and photocathode, respectively (Fig. S21, ESI†).

The photoanode and photocathode were integrated into a parallelly illuminated coplanar system for performing unbiased solar water splitting, as illustrated in Fig. S22 (ESI†). Each photoelectrode with varying sizes of 2 cm × 2 cm, 5 cm × 5 cm, and 8 cm × 8 cm was prepared to demonstrate the size-dependent STH efficiency of photoelectrodes, and the active area was defined to be 0.8 cm^2, 12 cm^2, and 30 cm^2, respectively (Fig. S23, ESI,† see Experimental Section for detailed sample preparation). To operate both devices in a single electrolyte chamber, 0.5 M KPi (pH 7) was selected as the optimum electrolyte. In Fig. 6(a–c), the champion LSV curves, separately obtained from the photoanode and photocathode with different device sizes are superimposed to determine the anticipated operation point of the unbiased device. The intersection point was determined to be 20.60 mA cm^{-2} at 0.82 V_{RHE}, 18.87 mA cm^{-2} at 0.74 V_{RHE}, and 15.05 mA cm^{-2} at 0.80 V_{RHE} for 2 cm × 2 cm (0.8 cm^2), 5 cm × 5 cm (12 cm^2), and 8 cm × 8 cm (30 cm^2) devices, respectively. It should be noted that the expected operation current had to be halved because of the coplanar configuration. The actual performance assessment of the parallelly illuminated coplanar LHP-based photoelectrodes was conducted using a two-electrode configuration in which both the photoanode and photocathode were subjected to 1-sun dual illumination in 0.5 M KPi (Fig. 6(d–f)). The voltage scanning ranged from −0.8 to 0.2 V. The total illuminated active area for 2 cm × 2 cm, 5 cm × 5 cm, and 8 cm × 8 cm coplanar devices was 1.6 cm^2, 24 cm^2, and 60 cm^2, respectively, since each photoanode was paired with a photocathode to operate under unbiased conditions. Under unbiased conditions (*i.e.*, 0 V), the parallelly illuminated coplanar LHP-based photoelectrodes with varying sizes delivered a photocurrent density of 10.64 mA cm^{-2}, 9.91 mA cm^{-2}, and 8.04 mA cm^{-2}, respectively, which closely matched the expected operation photocurrent density. From the obtained photocurrent density, the STH efficiency was calculated using the following equation:

$$STH(\%) = \frac{1.23 V \times J(mA\,cm^{-2})}{P_{in}(mW\,cm^{-2})} \qquad (2)$$

where J is the photocurrent density and P_{in} is the power of the incident light. The resulting STH efficiency was 13.09% (1.6 cm^2-sized device), 12.19% (24 cm^2-sized device), and 9.89% (60 cm^2-sized device), respectively, surpassing previously reported values of large-scale unbiased PEC photoelectrodes (Fig. S24, ESI†).[55] Furthermore, the parallelly illuminated coplanar LHP-based photoelectrodes exhibited an approximately 1 V

anodic shift compared to the *J–V* curve of the perovskite-based photoanode in 0.5 M KPi. This suggests that the perovskite-based photocathode successfully contributed a photovoltage of 1 V for unbiased solar water splitting, which was in agreement with the V_{OC} value obtained from the CHAI-bathed n–i–p structured PSC.

The H$_2$ production rate of each device was measured through gas chromatography as a function of operation time under unbiased conditions (Fig. 6(g–i)). The measured quantity of the H$_2$ gas was consistent with the theoretical value, revealing a 90–100% Faradaic efficiency. The actual H$_2$ production rate was 195.41 μmol h^{-1} cm^{-2}, 168.25 μmol h^{-1} cm^{-2}, and 146.56 μmol h^{-1} cm^{-2} for the varying-sized devices of 2 cm × 2 cm (1.6 cm^2), 5 cm × 5 cm (24 cm^2), and 8 cm × 8 cm (60 cm^2), respectively. The Faradaic efficiency for H$_2$ production from different-sized devices was also determined to be 98.50%, 91.04%, and 97.78%, respectively. Our devices showed outstanding H$_2$ production rates compared to other state-of-the-art unbiased PEC water splitting devices (Fig. S25, ESI†). Furthermore, the O$_2$ evolution rate of each device was measured through gas chromatography as a function of operation time under unbiased conditions (Fig. S26, ESI†). The measured quantity of O$_2$ gas was consistent with the theoretical value, also revealing a Faradaic efficiency of 90–100%. The actual O$_2$ production rate was 100.16 μmol h^{-1} cm^{-2}, 90.32 μmol h^{-1} cm^{-2}, and 77.98 μmol h^{-1} cm^{-2} for the varying sized devices of 2 cm × 2 cm (1.6 cm^2), 5 cm × 5 cm (24 cm^2), and 8 cm × 8 cm (60 cm^2), respectively. The long-term stability of unbiased photoelectrodes was chronoamperometrically evaluated under continuous illumination. As shown in Fig. 6(j–l), the 2 cm × 2 cm (1.6 cm^2)-sized coplanar LHP-based device retained 77% of its original STH efficiency after 28 h, while 85% of its initial STH efficiency was maintained after 30 h for the device with a size of 5 cm × 5 cm (24 cm^2). In addition, 8 cm × 8 cm (60 cm^2)-sized coplanar photoelectrodes retained 79% of its original STH efficiency after 24 h. To the best of our knowledge, our devices are outperforming all the previously reported operational stabilities for large-scale PEC devices (Fig. S27, ESI†). Encouraged by such results, we further upscaled our devices to 10 cm × 10 cm (active area size of 50 cm^2) and evaluated the device performance and stability (Fig. S28, ESI†). The champion LSV curves obtained from the photoanode and photocathode showed that the intersection point was at 4.81 mA cm^{-2} at 0.66 V_{RHE}. The parallelly illuminated coplanar LHP-based photoelectrodes (total active area 100 cm^2) delivered a photocurrent density of 2.51 mA cm^{-2}, which was close to the expected operation photocurrent density. The resulting STH efficiency was 3.09% which is the highest value considering the illuminated area per single unit cell (Fig. S23b, ESI†). The operational stability of 10 cm × 10 cm-sized devices was also extraordinary when considering their size, retaining 78% of initial current density after 7 h. Thus, it can be concluded that the CHAI bathing method is highly suitable for fabricating high-quality large-scale LHP films, successfully achieving the highest operation photocurrent, hydrogen production rate, and operational stability among PEC-based tandem devices without

This journal is © The Royal Society of Chemistry 2024

Energy Environ. Sci., 2024, **17**, 3604–3617 | **3613**

concentrated solar irradiation. The proposed strategy provides a pathway for the mass production of solar hydrogen through large-area LHP-based photoelectrodes.

Conclusions

In summary, we fabricated high-quality large-area LHP films for unbiased PEC water splitting with an antisolvent containing a defect passivation additive (*i.e.*, CHAI). During CHAI bathing, CHA^+ ions were incorporated into the wet perovskite film, where they interacted with PbI_6^{4-} octahedra to produce an intermediate phase. As a result of the formation of the intermediate phase, the nucleation of the wet precursor film was accelerated, and a uniform large-area LHP film with a smooth surface and enhanced crystallinity was formed. A systematic chemical analysis showed that CHAI molecules located at grain boundaries of LHP films effectively passivated the defects, leading to effective charge extraction and suppressing nonradiative recombination. Parallelly illuminated coplanar LHP-based electrodes (a photocathode and a photoanode), each with dimensions of 8 cm × 8 cm, were successfully operated under unbiased conditions. The resulting device exhibited a significantly high STH efficiency of 9.89% with a T_{80} of 24 h. The resulting device also exhibited the highest operation photocurrent among large-scale unassisted PEC tandem devices reported to date. Finally, the H_2 production rate of the coplanar device reached 145.56 μmol h^{-1} cm^{-2}, which is comparable to that of state-of-the-art unbiased PEC devices. Our work presents a new, simple, and highly versatile strategy for the fabrication of efficient and stable large-area LHP-based photoelectrodes for use in the mass production of solar hydrogen.

Experimental

Materials

Formamidinium iodide (FAI, > 99.99%), cyclohexylammonium iodide (CHAI, > 99.99%), and methylammonium bromide (MABr, > 99.99%) were purchased from Greatcell Solar (Queanbeyan, Australia). $PbBr_2$ (99.999%, trace metals basis), PbI_2 (99.99%, trace metals basis), lithium bis(fluorosulfonyl)imide (Li-TFSI, 98%), diethyl ether (DEE, anhydrous, ≥99.7%), dimethylformamide (DMF, anhydrous, 99.8%), dimethyl sulfoxide (DMSO, anhydrous, ≥99.9%), acetonitrile (anhydrous, 99.8%), chlorobenzene (anhydrous, 99.8%), CsI (99.999%, trace metals basis), $SnCl_2·2H_2O$ (99.99%, trace metals basis), 4-*tert*-butylpyridin (TBP, 96%), and 2, 2′,7,7′-tetrakis(*N*,*N*-dip-methoxyphenylamine)-9,9′-spirobifluorene (spiro-OMeTAD) were purchased from Sigma–Aldrich (St. Louis, MO, USA). All the chemicals were used as received, without any modification.

Device fabrication

A fluorine-doped tin oxide (FTO) substrate was etched using laser-etching equipment (Korthem Science, Korea). The FTO was sonicated with deionized (DI) water, acetone, and ethyl alcohol for 15 min each, followed by O_2 treatment for 10 min. For the fabrication of the SnO_2 electron transport layer, 275 mg of $SnCl_2·2H_2O$, 1.25 g of urea, 1.25 mL of HCl, and 25 mL of TGA were dissolved in DI water, and FTO substrates were placed in a chemical bath for 1.5 h. After the reaction, the substrates were sonicated with IPA and DI water for 15 min each and annealed at 170 °C for 1 h. The $(FAPbI_3)_{0.95}$-$(MAPbBr_3)_{0.05}$ perovskite precursor solution was prepared by mixing 1.4 M FAI, 1.4 M PbI_2, 0.023 M MABr, 0.023 M $PbBr_2$, 0.023 M CsI, and 0.5 M MACl in a mixed solvent of NMP and DMF at a ratio of 9 : 2. The precursor solutions were spin-coated onto glass/FTO/SnO_2 substrates by using a two-step process (1200 rpm for 12 s, 5000 rpm for 20 s). For a 10 cm × 10 cm device, the substrate was sequentially spin-coated at 1200 rpm for 12 s, 3000 rpm for 20 s. For the preparation of control films, the as-coated films were immersed into DEE antisolvent for 10 s, while CHAI dissolved in IPA (3 mg ml^{-1}) was poured into the DEE bath for the fabrication of CHAI-bathed films, followed by annealing at 100 °C for 50–60 min. For bar-coated films, the same precursor solutions were treated with a coating speed of 15 mm s^{-1} using a bar-coater (KP-3000VH, Kipae, Korea), followed by an identical antisolvent bathing and annealing process. The HTL precursor consisted of 72 mg of spiro-OMeTAD, 17.5 μL of a Li-TFSI solution (520 mg of Li-TFSI in 1 mL of acetonitrile), and 28.8 μL of TBP in 1.2 mL of chlorobenzene ratios of 0.54 and 3.3. After cooling the films, the HTL precursor was spin-coated at 3000 rpm for 30 s. The whole film deposition process was conducted inside a dry room where the humidity was strictly controlled (RH 5–10%). Finally, a 70 nm thick Au electrode was deposited using a thermal evaporator. To fabricate CHAI-FAI containing an intermediate phase, the precursor solution was prepared by mixing FAI, CHAI, and PbI_2 in a 0.5 : 0.5 : 2 molar ratio in 1 mL of NMP solvent. The precursor solution was spin-coated onto glass/FTO/SnO_2 substrates by using a two-step process (1200 rpm for 12 s, 3000 rpm for 20 s), without annealing. NiFe-LDH@Ni foam was hydrothermally synthesized. $Ni(NO_3)_2·6H_2O$ (0.3 g), $Fe(NO_3)_3·9H_2O$ (0.38 g), and urea (0.6 g) were dissolved in 70 mL of DI water under sonication for 15 min. The hydrothermal synthesis was conducted with a Teflon-lined stainless steel autoclave containing the solution, and the obtained Ni foam was annealed for 12 h at 120 °C. The resulting Ni foams were washed with DI water and acetone for 5 min each and dried for 24 h at 80 °C. The cocatalyst was attached to the Ni foil with silver paste (Elcoat). On the photocathode, a Cu tape was attached to the Au layer, and a Cu wire was then attached using silver paste. The HER catalyst was deposited onto the active area through blade coating of Pt paste; the Pt paste was prepared using Pt powder with 20% carbon black (Alfa Aesar; 20 mg), DI (0.75 ml), IPA (0.25 ml), and Nafion (Sigma–Aldrich, 0.2 mL). The printed catalyst was dried in ambient air for 24 h.

Film characterization

The phase evolution of the perovskite film was examined through XRD (Rigaku MiniFlex 600, The Woodlands, TX, USA). The surface morphology of the annealed samples was

3614 | *Energy Environ. Sci.*, 2024, **17**, 3604–3617

This journal is © The Royal Society of Chemistry 2024

determined *via* field emission SEM (JSM-7800F, JEOL Ltd, Japan) and contact-mode AFM (NX10 atomic force microscope, Park Systems, Korea). KPFM was conducted with an Au-coated Si tip (SI-DF3-A, $f = 23$–31 kHz) to obtain the contact potential difference for the device configuration of glass/FTO/perovskite under dark conditions. An external open-circuit DC bias was applied to the tips, while the FTO was grounded. FTIR spectra of the samples were measured with an FTIR spectrometer (Vertex 70, Bruker, MA, USA) in ambient air with powder sampling (KBr). The ^{1}H-NMR spectra of the annealed samples were measured with a 300 MHz FT-NMR spectrometer (AVANCE III HD 300). ToF-SIMS measurements (model TOF-SIMS V, ION-TOF GmbH, Germany) were conducted with pulsed primary ions from a Cs^+ (1 keV, 56.8 nA) liquid-metal ion gun for the sputtering and with Bi_1^+ and Bi_3^+ pulsed primary ion beam for analysis (30 keV). XPS depth profiling (K-Alpha, Thermo Scientific, UK) was performed with a monochromated Al Kα line, a voltage of 12 kV X-ray source, and a current of 3 mA, and an Ar ion gun with 500 eV power was employed for etching. Raman mapping images of as-bathed films were obtained with a confocal Raman microscope (Alpha300 Apyron, WITec, Germany). Steady-state photoluminescence (PL) was measured using a Raman microscope with an excitation wavelength of 532 nm.

Photovoltaic measurements

The photovoltaic (PV) performance of the PSCs was evaluated using a solar simulator (Sol3A Class AAA, Oriel Instruments, Stratford, CT, USA) under 1.5 AM and 1-sun conditions (100 mW cm^{-2}); the calibration was performed with a Si reference cell (Newport Corporation, Irvine, USA). The active area (0.06 cm^2) of the PSC was covered with an aperture mask and then exposed to light. For each sample, 20 devices were used for statistical analysis. The current was measured by scanning over a range of -0.1 to 1.5 V at a rate of 0.50 V s^{-1}, with a dwell time of 50 ms at each point. Before SCLC measurements, a 5 V pulse voltage was applied for 1 min to exclude the ionic conductivity of perovskite films. EQE spectra were obtained using a quantum-efficiency measurement system (QEX10, PV Measurements, Inc.). All the PV measurements were performed under an ambient atmosphere (RH 15–20%, 25 °C).

PEC measurements

For LSV measurements, the exposed area (illuminated area) of the LHP photoelectrodes was 0.8 cm^2, and the catalytic active area was identical to the exposed photoelectrode area. For large-area PEC devices, the exposed area and active area were fixed at 12 cm^2 (3 cm $\times$ 4 cm for the photoanode, 2.4 cm $\times$ 5 cm for the photocathode), 30 cm^2 (5 cm $\times$ 6 cm for the photoanode, 3.75 cm $\times$ 8 cm for the photocathode), and 50 cm^2 (6.5 cm $\times$ 7.7 cm for the photoanode, 5 cm $\times$ 10 cm for the photocathode), respectively, with the overall device size being 25 (5 $\times$ 5) cm^2, 64 (8 $\times$ 8) cm^2, and 100 (10 $\times$ 10) cm^2. For LSV and chronoamperometry measurements, a three-electrode system, with a Pt wire as the counter electrode and Ag/AgCl/KCl

(4 m) as the reference electrode in either 0.5 M KPi (pH 7), 1 M KOH solution (pH 14), or 0.5 M H_2SO_4 solution (pH 1), was used under simulated solar light illumination (AM 1.5G; DTX, Korea). For all PEC measurements, the wire was connected to a potentiostat (SI 1287, Solartron, UK) to control the potential and current. Furthermore, the applied potentials were evaluated with respect to the RHE value for comparison with previously reported values; the expression used for the evaluation was $E_{RHE} = E_{Ag/AgCl} + 0.059$ pH $+ 0.197$. The ABPE was calculated from the LSV curve by using the following equation:

$$\text{ABPE}\,(\%) = \left(\frac{J^{OER} \times (1.23 - V)}{P_0} \right) \times 100\% \qquad (3)$$

where J^{OER} is the measured photocurrent density, V is the applied bias, and P_0 is the incident illumination power density (*i.e.*, AM 1.5G, 100 mW cm^{-2}). Gas chromatography (6500GC system, YL Instrument, Anyang, Korea) was performed with a pulsed discharge detector and a molecular sieve column to confirm the evolution of H_2 and O_2. Rubber bulkheads and Parafilm were used to seal the quartz for preventing gas leakage. For the calculation of H_2 and O_2 production rates, the photocurrent delivered by the coplanar LHP-based device was divided by the Faraday constant; it was assumed that two electrons are required for H_2 evolution and four holes are needed for O_2 evolution (Faradaic efficiency was derived from Fig. 6(g–i) and Fig. S26, ESI,† respectively).

Conflicts of interest

There are no conflicts to declare.

Acknowledgements

Notes and references

1 J. H. Kim, D. Hansora, P. Sharma, J. W. Jang and J. S. Lee, *Chem. Soc. Rev.*, 2019, **48**, 1908–1971.

2 W. Yang, R. R. Prabhakar, J. Tan, S. D. Tilley and J. Moon, *Chem. Soc. Rev.*, 2019, **48**, 4979–5015.

3 H. Song, S. Q. Luo, H. M. Huang, B. W. Deng and J. H. Ye, *ACS Energy Lett.*, 2022, **7**, 1043–1065.

4 S. Y. Chae, H. Jung, H. S. Jeon, B. K. Min, Y. J. Hwang and O. S. Joo, *J. Mater. Chem. A*, 2014, **2**, 11408–11416.

5 J. W. Yun, J. W. Tan, Y. K. Jung, W. Yang, H. Lee, S. Ma, Y. S. Park, C. U. Lee, W. Z. Niu, J. Lee, K. Kim, S. D. Tilley, A. Walsh and J. Moon, *ACS Energy Lett.*, 2022, **7**, 1392–1402.

6 H. Lee, S. Ma, S. Oh, J. W. Tan, C. U. Lee, J. Son, Y. S. Park, J. Yun, G. Jang and J. Moon, *Small*, 2023, **19**, 2304166.

This journal is © The Royal Society of Chemistry 2024

Energy Environ. Sci., 2024, **17**, 3604–3617 | **3615**

7 Y. S. Park, J. W. Lee, H. Lee, J. Yun, G. Jang, J. Lee, S. Son, C. U. Lee, C. S. Jeong, S. Moon, S. Lee, H. I. Kim and J. Moon, *Adv. Energy Mater.*, 2023, **13**, 2301166.

8 J. Joo, T. Kim, J. Lee, S. I. Choi and K. Lee, *Adv. Mater.*, 2019, **31**, 1806682.

9 L. F. Pan, J. H. Kim, M. T. Mayer, M. K. Son, A. Ummadisingu, J. S. Lee, A. Hagfeldt, J. S. Luo and M. Grätzel, *Nat. Catal.*, 2018, **1**, 412–420.

10 S. G. Shim, J. Tan, H. Lee, J. Park, J. Yun, Y. S. Park, K. Kim, J. Lee and J. Moon, *Chem. Eng. J.*, 2022, **430**, 133061.

11 J. Tan, W. Yang, H. Lee, J. Park, K. Kim, O. S. Hutter, L. J. Phillips, S. Shim, J. Yun, Y. Park, J. Lee, J. D. Major and J. Moon, *Appl. Catal., B*, 2021, **286**, 119890.

12 A. M. K. Fehr, T. G. Deutsch, F. M. Toma, M. S. Wong and A. D. Mohite, *ACS Energy Lett.*, 2023, **8**, 4976–4983.

13 S. Khamgaonkar, Q. Y. Chen, K. Musselman and V. Maheshwari, *J. Mater. Chem. A*, 2023, **11**, 20079–20088.

14 H. Choi, S. Seo, C. J. Yoon, J. B. Ahn, C. S. Kim, Y. S. Jung, Y. Kim, F. M. Toma, H. Kim and S. H. Lee, *Adv. Sci.*, 2023, **10**, 2303106.

15 J. Yun, H. Lee, Y. S. Park, W. Jeong, C. S. Jeong, J. Lee, J. Lee, J. Tan, S. Ma, G. Jang, C. U. Lee, S. Moon, H. Im, S. Lee, D. Y. Yee, J. H. Kim and J. Moon, *Adv. Energy Mater.*, 2023, **13**, 2301693.

16 A. M. K. Fehr, A. Agrawal, F. Mandani, C. L. Conrad, Q. Jiang, S. Y. Park, O. Alley, B. R. Li, S. Sidhik, I. Metcalf, C. Botello, J. L. Young, J. Even, J. C. Blancon, T. G. Deutsch, K. Zhu, S. Albrecht, F. M. Toma, M. C. Wong and A. D. Mohite, *Nat. Commun.*, 2023, **14**, 3797.

17 Z. N. Song, C. W. Li, L. Chen, K. Dolia, S. Fu, N. N. Sun, Y. Li, K. Wyatt, J. L. Young, T. G. Deutsch and Y. F. Yan, *ACS Energy Lett.*, 2023, **8**, 2611–2619.

18 H. Choi, Y. Y. Kim, S. Seo, Y. Jung, S. M. Yoo, C. S. Moon, N. J. Jeon, S. Lee, K. Lee, F. M. Toma, J. Seo and S. Lee, *Adv. Energy Mater.*, 2023, **13**, 2300951.

19 H. Choi, S. Seo, J. H. Kim, J. H. Lee, S. Kim, G. Piao, H. Park, K. Lee and S. Lee, *J. Mater. Chem. A*, 2023, **11**, 993.

20 J. Park, J. Lee, H. Lee, H. Im, S. Moon, C. S. Jeong, W. Yang and J. Moon, *Small*, 2023, **19**, 2300174.

21 J. X. Yang, E. L. Lim, L. Tan and Z. H. Wei, *Adv. Energy Mater.*, 2022, **12**, 2200975.

22 N. G. Park and K. Zhu, *Nat. Rev. Mater.*, 2020, **5**, 333–350.

23 L. G. Xu, H. D. Ji, W. Qiu, X. Wang, Y. Liu, J. H. Li, J. Li, X. Zhang, D. Q. Zhang, J. X. Wang, Y. Tao, M. C. Li and R. F. Chen, *Adv. Mater.*, 2023, **35**, 2301752.

24 D. Hansora, D. Cherian, R. Mehrotra, J. W. Jang and J. S. Lee, *Joule*, 2023, **7**, 884–919.

25 B. Liu, S. J. Wang, G. Zhang, Z. C. Gong, B. Wu, T. Wang and J. L. Gong, *Chem. Soc. Rev.*, 2023, **52**, 4644–4671.

26 G. R. Adams, V. O. Eze, L. B. Carani, A. Pino, C. Jolowsky and O. I. Okoli, *RSC Adv.*, 2020, **10**, 18139–18146.

27 G. Jang, H. C. Kwon, S. Ma, S. C. Yun, H. Yang and J. Moon, *Adv. Energy Mater.*, 2019, **9**, 1901719.

28 G. Jang, S. Ma, H. C. Kwon, S. Goh, H. Ban, J. Lee, C. U. Lee and J. Moon, *Chem. Eng. J.*, 2021, **423**, 130078.

29 N. Kwon, J. Lee, M. J. Ko, Y. Y. Kim and J. Seo, *Nano Convergence*, 2023, **10**, 1–18.

30 Y. Y. Kim, T. Y. Yang, R. Suhonen, A. Kemppainen, K. Hwang, N. J. Jeon and J. Seo, *Nat. Commun.*, 2020, **11**, 5146.

31 F. Gao, Y. Zhao, X. W. Zhang and J. B. You, *Adv. Energy Mater.*, 2020, **10**, 1902650.

32 Z. F. Wu, E. B. Bi, L. K. Ono, D. B. Li, O. M. Bakr, Y. F. Yan and Y. B. Qi, *Nano Energy*, 2023, **115**, 108731.

33 S. Jeong, S. Seo, H. Yang, H. Park, S. Shin, H. Ahn, D. Lee, J. H. Park, N. G. Park and H. Shin, *Adv. Energy Mater.*, 2021, **11**, 2102236.

34 S. C. Yun, S. Ma, H. C. Kwon, K. Kim, G. Jang, H. Yang and J. Moon, *Nano Energy*, 2019, **59**, 481–491.

35 J. W. Lee, Z. H. Dai, C. Lee, H. M. Lee, T. H. Han, N. De Marco, O. Lin, C. S. Choi, B. Dunn, J. Koh, D. Di Carlo, J. H. Ko, H. D. Maynard and Y. Yang, *J. Am. Chem. Soc.*, 2018, **140**, 6317–6324.

36 C. C. Wu, D. Wang, Y. Q. Zhang, F. D. Gu, C. H. Liu, N. Zhu, W. Luo, D. Han, X. Guo, B. Qu, S. F. Wang, Z. Q. Bian, Z. J. Chen and L. X. Xiao, *Adv. Funct. Mater.*, 2019, **29**, 1902974.

37 A. A. Petrov, N. Pellet, J. Y. Seo, N. A. Belich, D. Y. Kovalev, A. V. Shevelkov, E. A. Goodilin, S. M. Zakeeruddin, A. B. Tarasov and M. Graetzel, *Chem. Mater.*, 2017, **29**, 587–594.

38 W. C. Xiang, J. H. Zhang, S. Z. Liu, S. Albrecht, A. Hagfeldt and Z. W. Wang, *Joule*, 2022, **6**, 315–339.

39 E. Kucharska, J. Hanuza, A. Ciupa, M. Maczka and L. Macalik, *Vib. Spectrosc.*, 2014, **75**, 45–50.

40 M. A. Pérez-Osorio, Q. Q. Lin, R. T. Phillips, R. L. Milot, L. M. Herz, M. B. Johnston and F. Giustino, *J. Phys. Chem. C*, 2018, **122**, 21703–21717.

41 S. Ruan, D. P. McMeekin, R. Fan, N. A. S. Webstereb, H. Ebendorff-Heidepriem, Y. B. Cheng, J. F. Lu, Y. L. Ruan and C. R. McNeill, *J. Phys. Chem. C*, 2020, **124**, 2265–2272.

42 D. Hughes, S. M. P. Meroni, J. Barbé, D. Raptis, H. K. H. Lee, K. C. Heasman, F. Lang, T. M. Watson and W. C. Tsoi, *Energy Technol.*, 2021, **9**, 2100928.

43 X. Hou, S. M. Huang, O. Y. Wei, L. K. Pan, Z. Sun and X. H. Chen, *ACS Appl. Mater. Interfaces*, 2017, **9**, 35200–35208.

44 R. H. Zheng, S. S. Zhao, H. Zhang, H. Y. Li, J. Zhuang, X. C. Liu, H. M. Li and H. Y. Wang, *Sol. Energy*, 2021, **224**, 472–479.

45 L. F. Zheng, L. A. Shen, Z. Fang, P. Q. Song, W. J. Tian, J. F. Chen, K. K. Liu, Y. J. Luo, P. Xu, J. X. Yang, C. B. Tian, L. Q. Xie and Z. H. Wei, *Adv. Energy Mater.*, 2023, **13**, 2301066.

46 W. C. Yang, B. Ding, Z. D. Lin, J. S. Sun, Y. Y. Meng, Y. Ding, J. Sheng, Z. H. Yang, J. C. Ye, P. J. Dyson and M. K. Nazeeruddin, *Adv. Mater.*, 2023, **35**, 2302071.

47 C. Zhang, H. Y. Li, H. Gong, Q. X. Zhuang, J. Z. Chen and Z. G. Zang, *Energy Environ. Sci.*, 2023, **16**, 3825–3836.

48 L. H. Zhu, X. Zhang, M. J. Li, X. N. Shang, K. X. Lei, B. X. Zhang, C. Chen, S. J. Zheng, H. W. Song and J. Z. Chen, *Adv. Energy Mater.*, 2021, **11**, 2100529.

49 J. C. Yang, W. J. Tang, R. H. Yuan, Y. Chen, J. Wang, Y. H. Wu, W. J. Yin, N. Y. Yuan, J. N. Ding and W. H. Zhang, *Chem. Sci.*, 2021, **12**, 2050–2059.

50 G. D. Li, J. Song, J. H. Wu, Z. Y. Song, X. B. Wang, W. H. Sun, L. Q. Fan, J. M. Lin, M. L. Huang, Z. Lan and P. Gao, *ACS Energy Lett.*, 2021, **6**, 3614–3623.

51 S. Tan, T. Y. Huang, I. Yavuz, R. Wang, M. H. Weber, Y. P. Zhao, M. Abdelsamie, M. E. Liao, H. C. Wang, K. Huynh, K. H. Wei, J. J. Xue, F. Babbe, M. S. Goorsky, J. W. Lee, C. M. Sutter-Fella and Y. Yang, *J. Am. Chem. Soc.*, 2021, **143**, 6781–6786.

52 A. L. Hassan, Z. J. Wang, Y. H. Ahn, M. Azam, A. A. Khan, U. Farooq, M. Zubair and Y. Cao, *Nano Energy*, 2022, **101**, 107579.

53 V. M. Le Corre, E. A. Duijnstee, O. El Tambouli, J. M. Ball, H. J. Snaith, J. Lim and L. J. A. Koster, *ACS Energy Lett.*, 2021, **6**, 1087–1094.

54 F. Wu, S. Mabrouk, M. M. Han, Y. H. Tong, T. S. Zhang, Y. C. Zhang, R. S. Bobba and Q. Qiao, *J. Energy Chem.*, 2023, **76**, 414–420.

55 D. Hansora, J. Yoo, R. Mehrotra, W. Byun, D. Lim, Y. Kim, E. Noh, H. Lim, J. Jang, S. Seok and J. Lee, *Nat. Energy*, 2024, **9**, 272–284.

This journal is © The Royal Society of Chemistry 2024

Energy Environ. Sci., 2024, **17**, 3604–3617 | **3617**